MARTEC™

Smart Solutions for Engineering,
Science and Computing

Cylindrical Explosive Dispersal of Metal Particles: Predictive Calculations in Support of Experimental Trials

Martec Technical Report # TR-07-66

December 2007

Prepared for:

Dr. Yasuyuki Horie
US Air Force Research Laboratory
Eglin Air Force Base
Florida, USA
32542

Smart Solutions for Engineering,
Science & Computing

Martec Limited
1888 Brunswick Street, Suite 400
Halifax, Nova Scotia B3J 3J8 Canada

tel. 902.425.5101
fax. 902.421.1923
email. info@martec.com
www.martec.com

REPORT DOCUMENTATION PAGE

AFRL-SR-AR-TR-09-0256

PLEASE DO NOT RETURN YOUR FORM TO THE ABOVE ADDRESS.

1. REPORT DATE *(DD-MM-YYYY)*	2. REPORT TYPE	3. DATES COVERED (From – To)
08 JUN 2008	Final Technical Report	19 JUN 2006 – 31 MAY 2007

4. TITLE AND SUBTITLE
Modeling Fragmentation and Reactive Dispersal of Explosively Loaded Metals

5a. CONTRACT NUMBER

5b. GRANT NUMBER
FA9550-06-1-0551

5c. PROGRAM ELEMENT NUMBER

6. AUTHOR(S)
Robert C. Ripley

5d. PROJECT NUMBER

5e. TASK NUMBER

5f. WORK UNIT NUMBER

7. PERFORMING ORGANIZATION NAME(S) AND ADDRESS(ES)
US Air Force Research Laboratory
Eglin Air Force Base
Florida, USA 32542

Martec Limited
1888 Brunswick St., Suite 400
Halifax, Nova Scotia B3J 3J8 Canada
Tel: 902.425.5101

8. PERFORMING ORGANIZATION REPORT NUMBER

9. SPONSORING/MONITORING AGENCY NAME(S) AND ADDRESS(ES)
USAF/AFRL
AFOSR
875 North Randolph Street
Arlington VA 22203

10. SPONSOR/MONITOR'S ACRONYM(S)
AFOSR

11. SPONSORING/MONITORING AGENCY REPORT NUMBER
N/A

12. DISTRIBUTION AVAILABILITY STATEMENT

Distribution Statement A: Approved for public release. Distribution is unlimited.

13. SUPPLEMENTARY NOTES

14. ABSTRACT

The Explosive dispersal of densely-packed metal particles in cylindrical RDX-based charges was studied numerically in support of experimental trials. Simulations were conducted using a reactive multiphase fluid dynamic code. Fundamental studies using a large-scale explosive were performed to show scaling phenomena while avoiding potential initiation and critical diameter effects. Spherical tungsten particles were applied in high metal mass fraction cylindrical and spherical charges in two configurations: a particle matrix uniformly embedded in a solid explosive versus an annular shell of particles surrounding a high-explosive core. The effect of particle number density was investigated by varying the nominal particle diameter from 27 to 120 um while maintaining a constant metal mass fraction. Results were compared with steel particles to evaluate the influence of material density dispersal. Preliminary laboratory-scale simulations were performed using the anticipated experimental configuration for the High Explosives R&D facility at Eglin AFB trials. The effect of particle size and density were investigated, and information to assist in the experiments was obtained. Results were consistent with the fundamental study involving the large-scale explosives, particulary the shape of the cylindrical dispersed dense particle slug, and the relative performance of the large and small particles.

15. SUBJECT TERMS

16. SECURITY CLASSIFICATION OF:			17. LIMITATION OF ABSTRACT	18. NUMBER OF PAGES	19a. NAME OF RESPONSIBLE PERSON
a. REPORT	b. ABSTRACT	c. THIS PAGE			J. Fillerup
Unclassified	Unclassified	Unclassified	Unclassified		19b. TELEPONE NUMBER (*Include area code*) (703) 588.1777

REVISION CONTROL

REVISION	REVISION DATE

SIGNATURE PAGE

CYLINDRICAL EXPLOSIVE DISPERSAL OF METAL PARTICLES: PREDICITIVE CALCULATIONS IN SUPPORT OF EXPERIMENTAL TRIALS

Technical Report # TR-07-66
11 December 2007

Prepared by: Laura Donahue **Date:** Dec 11, 2007
Laura Donahue, P.Eng.
Research Engineer

Rob Ripley **Date:** DEC 11, 2007
Robert C. Ripley, P.Eng.
Research Engineer

Reviewed by: Rob Ripley **Date:** DEC 11, 2007
Robert C. Ripley, P.Eng.
Research Engineer

Approved by: David R Whitehouse **Date:** Dec 11, 2007
David R. Whitehouse, P.Eng.
Manager – Combustion Dynamics Group

EXECUTIVE SUMMARY

The explosive dispersal of densely-packed metal particles in cylindrical RDX-based charges was studied numerically in support of experimental trials. Simulations were conducted using a reactive multiphase fluid dynamic code.

Fundamental studies using a large-scale explosive were performed to show scaling phenomena while avoiding potential initiation and critical diameter effects. Spherical tungsten particles were applied in high metal mass fraction cylindrical and spherical charges in two configurations: a particle matrix uniformly embedded in a solid explosive versus an annular shell of particles surrounding a high-explosive core. The effect of particle number density was investigated by varying the nominal particle diameter from 27 to 120 μm while maintaining a constant metal mass fraction. Results were compared with steel particles to evaluate the influence of material density on dispersal.

Preliminary laboratory-scale simulations were performed using the anticipated experimental configuration for the High Explosives R&D facility at Eglin AFB trials. The effect of particle size and density were investigated, and information to assist in the experiments was obtained. Results were consistent with the fundamental study involving the large-scale explosives, particularly the shape of the cylindrical dispersed dense particle slug, and the relative performance of the large and small particles.

Funding for this project was provided by the U.S. Air Force Office of Scientific Research under Grant FA9550-06-1-0551.

TABLE OF CONTENTS

1.0 INTRODUCTION 1

2.0 NUMERICAL METHODS 2

3.0 LARGE SCALE EXPLOSIVE DISPERSAL 3

3.1 SPHERICAL EXPLOSIVE DISPERSAL 4
3.1.1 Particle Morphology Effects 4
3.1.2 Particle Distribution Effects 4
3.2 CYLINDRICAL PARTICLE DISPERSAL 6

4.0 PRELIMINARY LABORATORY-SCALE INVESTIGATIONS 10

4.1 EXPLOSIVE DETAILS 10
4.2 A5/W-27 RESULTS 11
4.3 A5/W-120 RESULTS 14
4.4 A5/AL-31 RESULTS 17

5.0 DISCUSSION/CONCLUSIONS 21

6.0 REFERENCES 22

LIST OF FIGURES

FIGURE 1: SCHEMATIC OF MATRIX AND SHELL CONFIGURATIONS. INITIATION LOCATIONS ARE INDICATED BY RED CIRCLES. 3

FIGURE 2: WAVE DIAGRAM FOR 2.5 KG SPHERICAL MATRIX CHARGES. THICK LINES, 120 μM; THIN LINES, 27 μM; SOLID LINES, TUNGSTEN; DASHED LINES, STEEL; BLACK LINES (NO SYMBOLS), FIREBALL; LIGHT BLUE LINES, SHOCK; AND, BLACK LINES WITH SYMBOLS, PARTICLE FRONT. 4

FIGURE 3: WAVE DIAGRAM FOR 2.5 KG SPHERICAL TUNGSTEN MATRIX AND SHELL CONFIGURATION CHARGES. THICK LINES, 120 μM; THIN LINES, 27 μM; SOLID LINES, MATRIX; DASHED LINES, SHELL; BLACK LINES, FIREBALL; LIGHT BLUE LINES, SHOCK; AND, BLACK LINES WITH SYMBOLS, PARTICLE FRONT. 5

FIGURE 4: WAVE DIAGRAM FOR CYLINDRICAL DISPERSAL OF 2.5 KG TUNGSTEN CHARGES (27 μM DIAMETER). THICK LINES, CYLINDRICAL CHARGE; THIN LINES, SPHERICAL CHARGE; SOLID LINES, MATRIX; DASHED LINES, SHELL; BLACK LINES (NO SYMBOLS), FIREBALL; LIGHT BLUE LINES, SHOCK; AND, BLACK LINES WITH SYMBOLS, PARTICLE FRONT. 6

FIGURE 5: FLUID DENSITY (COLOUR) AND PARTICLE CONCENTRATION (LINES – LOG) FOR 27 μM TUNGSTEN PARTICLES IN 2.5 KG (TOP) SHELL AND (BOTTOM) MATRIX CONFIGURATIONS. SHADING INDICATES STRENGTH OF DENSITY GRADIENT. 8

FIGURE 6: CONCENTRATION OF DISPERSED 27 μM TUNGSTEN PARTICLES IN 2.5 KG MATRIX AND SHELL CONFIGURATIONS AT (LEFT) T = 1.0 MS AND (RIGHT) T = 8.0 MS. 9

FIGURE 7: RADIAL VELOCITY DISTRIBUTION OF 27 μM TUNGSTEN PARTICLES IN 2.5 KG MATRIX AND SHELL CONFIGURATIONS AT (LEFT) T = 1.0 MS AND (RIGHT) T = 8.0 MS. 9

FIGURE 8: PREPARED EXPERIMENTAL CHARGES. 10

FIGURE 9: CHARGE DIMENSIONS IN MILLIMETRES. 10

FIGURE 10: EARLY-TIME EXPLOSIVE DETONATION AND PARTICLE DISPERSAL OF A5/W-27. FLOOD INDICATES PRESSURE LEVEL; SOLID LINES DENOTE PARTICLE CONCENTRATION OF 10 MG/M^3 TO 0.1 KG/M^3 (LOG SCALE). 11

FIGURE 11: EARLY-TIME PARTICLE SPEED PROFILE FOR A5/W-27. FLOOD INDICATES PARTICLE SPEED LEVEL; SOLID LINES DENOTE PARTICLE CONCENTRATION OF 10 MG/M^3 TO 0.1 KG/M^3 (LOG SCALE). 12

FIGURE 12: LATE-TIME PARTICLE DISPERSAL AND SHOCK PROPAGATION OF A5/W-27. FLOOD INDICATES FLUID PRESSURE LEVEL; SOLID LINES DENOTE PARTICLE CONCENTRATION OF 10 MG/M^3 TO 0.1 KG/M^3 (LOG SCALE). 13

FIGURE 13: LATE-TIME A5/W-27 PARTICLE SPEED. SOLID LINES DENOTE PARTICLE CONCENTRATION OF 10 MG/M^3 TO 0.1 KG/M^3 (LOG SCALE). 13

FIGURE 14: GAUGE HISTORIES FOR A5/W-27 (LEFT) PRESSURE AND (RIGHT) PARTICLE NUMBER DENSITY 14

FIGURE 15: EARLY-TIME EXPLOSIVE DETONATION AND PARTICLE DISPERSAL OF A5/W-120. FLOOD INDICATES FLUID PRESSURE LEVEL; SOLID LINES DENOTE PARTICLE CONCENTRATION OF 10 MG/M^3 TO 0.1 KG/M^3 (LOG). 15

FIGURE 16: EARLY-TIME PARTICLE SPEED PROFILE FOR A5/W-120. FLOOD INDICATES PARTICLE SPEED LEVEL; SOLID LINES DENOTE PARTICLE CONCENTRATION OF 10 MG/M^3 TO 0.1 KG/M^3 (LOG). 15

FIGURE 17: LATE-TIME PARTICLE DISPERSAL AND SHOCK PROPAGATION OF A5/W-120. FLOOD COLOUR INDICATES FLUID PRESSURE LEVEL; SOLID LINES DENOTE PARTICLE CONCENTRATION OF 10 MG/M^3 TO 0.1 KG/M^3 (LOG SCALE). 16

FIGURE 18: LATE-TIME A5/W-120 PARTICLE SPEED. SOLID LINES DENOTE PARTICLE CONCENTRATION OF 10 MG/M^3 TO 0.1 KG/M^3 (LOG SCALE). 16

FIGURE 19: GAUGE HISTORIES FOR A5/W-120 (LEFT) PRESSURE AND (RIGHT) PARTICLE NUMBER DENSITY 17

FIGURE 20: EARLY-TIME EXPLOSIVE DETONATION AND PARTICLE DISPERSAL OF A5/AL-31. FLOOD INDICATES FLUID PRESSURE LEVEL; SOLID LINES DENOTE PARTICLE CONCENTRATION OF 10 MG/M^3 TO 0.1 KG/M^3 (LOG SCALE). 18

FIGURE 21: EARLY-TIME PARTICLE SPEED PROFILE FOR A5/AL-31. FLOOD INDICATES PARTICLE SPEED LEVEL; SOLID LINES DENOTE PARTICLE CONCENTRATION OF 10 MG/M^3 TO 0.1 KG/M^3 (LOG SCALE). 18

FIGURE 22: LATE-TIME PARTICLE DISPERSAL AND SHOCK PROPAGATION OF A5/AL-31. FLOOD INDICATES FLUID PRESSURE LEVEL; SOLID LINES DENOTE PARTICLE CONCENTRATION OF 10 MG/M^3 TO 0.1 KG/M^3 (LOG SCALE). 19

FIGURE 23: LATE-TIME A5/AL-31 PARTICLE SPEED. SOLID LINES DENOTE PARTICLE CONCENTRATION OF 10 MG/M^3 TO 0.1 KG/M^3 (LOG SCALE). 19

FIGURE 24: GAUGE HISTORIES FOR A5/AL-31 (LEFT) PRESSURE AND (RIGHT) PARTICLE NUMBER DENSITY 20

LIST OF TABLES

TABLE 1: METALIZED EXPLOSIVE CHARGE COMPOSITION 3
TABLE 2: CHARGE DETAILS 11

1.0 INTRODUCTION

Some heterogeneous explosive formulations consist of a condensed explosive surrounded by a dense metal particle layer. The dispersal of inert particles from a high explosive charge is investigated numerically in the current work. The modeling is motivated by an experimental effort at the High Explosives R&D facility at Eglin AFB that aims to simulate dispersal and afterburning effects using dense metal particles as casing surrogates. Modeling calculations are used to predict the arrival time and duration of the dispersed particle cloud including its time-varying concentration and velocity. This information will allow optimal configuration of the diagnostics and optics in order to avoid the obscuring effects of the fireball while capturing particle kinetic effects in the near field. Inert particles are the focus of the present work to study fundamentals and to calibrate equipment, while avoiding complexities introduced by reactive particle luminescence and reaction products in the flow field.

2.0 NUMERICAL METHODS

All simulations are performed using *Chinook*, a 3D parallel unstructured mesh CFD code for the simulation of time-accurate explosive events. This code, developed by Martec Limited, has been validated and used for spherical inert particle dispersal [1], cylindrical reactive particle scenarios [2] and multiphase explosions [3] featuring high metal mass fractions.

The governing equations are the Euler equations for conservation of mass, momentum, energy, material concentrations and particle number density (number of particles per unit volume). It features the second-order HLLC approximate Riemann solver [4, 5] which is used for both the fluid and particle phases, each of which has independent velocity and temperature fields. The Godunov-type solver can handle all sound speeds in a generalized Riemann solver framework for the condensed explosive, multicomponent detonation products, granular material, discrete particle system and air. The particle model developed in [1] is used, capable of simulating the solid flow from solid continuum to a highly dilute particle system, with the associated variance in sound speed (from 0 m/s to 10^3 m/s). Gas-particle interactions are simulated using phase exchange source terms, which are based on traditional empirical correlations for drag (momentum), heat transfer (convection) and mass transfer (particle combustion). The governing equations and particle exchange source terms are described in [6, 7].

Equations of state (EOS) are required to model each material and to close the system of equations:

- Mie-Grüneisen EOS for condensed reactants [8] with Walsh and Christian temperature fitting [9]
- Jones-Wilkens-Lee (JWL) for gaseous detonation products [10]; explosive fitting parameters calculated using Cheetah [11]
- Ideal Gas Law for surrounding atmosphere and air-blast (gamma = 1.4)
- Phenomenological EOS for solid particles (both dense and dilute) [1]

To account for early-time particle loading, momentum acceleration factors for shock interaction with packed metal particles are employed. The near-field dense granular heterogeneous flow effect is included in the governing equations and drag model; in the far field, drag is the main driving force within the expanding detonation product gases and air.

3.0 LARGE SCALE EXPLOSIVE DISPERSAL

The effect of particle morphology and distribution were investigated through a series of 1D and 2D calculations. Although small-scale charges (25 – 250 g) are planned for the preliminary experiments at Eglin AFB, metalized explosive charge sizes of 2.5 and 20 kg are studied in this section to show dispersal phenomena while avoiding potential initiation and critical diameter effects. The explosive formulations considered are given in Table 1 (W = tungsten, Fe = steel).

Table 1: Metalized explosive charge composition

Comp	% vol.	% wt. A5/W	% wt. A5/Fe
A5 (98.5% RDX)	60.3	11.5	24.2
Metal	39.7	88.5	75.8

Figure 1 illustrates the charges investigated in the current study. In the first charge configuration, a matrix of metal particles is embedded uniformly in a solid high explosive, while in the second configuration an explosive core is surrounded by an annular shell of particles. Both 2.5 and 20 kg charges were analyzed. The charge outer diameters ranged from 5.7 to 9.0 cm for the 2.5 kg charge and from 11.4 to 18.0 cm for the 20 kg charge depending on configuration. The shell thickness was 10.3 and 21.0 mm in the 2.5 and 20 kg A5/tungsten spherical charges, respectively. For the cylinders, the charge length is twice the outer diameter. Because of the cylindrical charge aspect ratio, the spherical charge of the same mass has a smaller outer diameter.

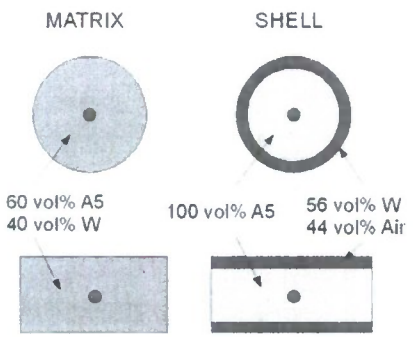

Figure 1: Schematic of matrix and shell configurations. Initiation locations are indicated by red circles.

3.1 SPHERICAL EXPLOSIVE DISPERSAL

3.1.1 Particle Morphology Effects

The effect of particle material and diameter on the dispersal dynamics was investigated through 1D calculations involving spherical charges containing 27 and 120 μm diameter tungsten and steel particles. The metal particles were distributed in a uniform matrix throughout the charge, with voids filled with A5 explosive. This configuration is similar to that studied by Zhang et al. [1].

Figure 2 illustrates the effect of particle diameter and material. Due to greater inertia, the dispersed front of larger particles remains at nearly constant velocity longer than that of the smaller particles, which decelerate and are overtaken by the shock front. Charges containing steel particles have a faster shock speed and larger fireball indicating less momentum and energy transfer to the particles in their acceleration and heating as compared to the heavier tungsten particles of the same size. However, because of the lower steel particle inertia, large steel particles are dispersed ahead of the tungsten particles until $r > 4.0$ m, and small steel particles pass the same size tungsten particles at $r = 1.3$ m for the same explosive fraction.

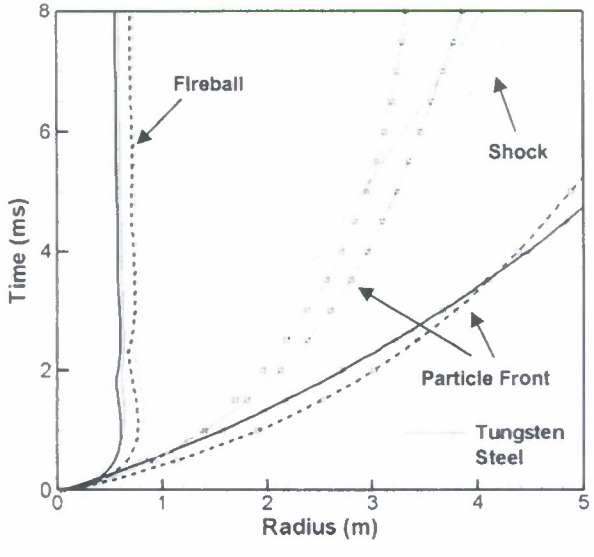

Figure 2: Wave diagram for 2.5 kg spherical matrix charges. Thick lines, 120 μm; thin lines, 27 μm; solid lines, tungsten; dashed lines, steel; black lines (no symbols), fireball; light blue lines, shock; and, black lines with symbols, particle front.

3.1.2 Particle Distribution Effects

The effect of the distribution of particles within the charge was investigated for the same weight fraction of tungsten to A5 as that of the matrix charge specified in Table 1. The matrix configuration was compared with an annular particle shell surrounding the explosive core

(Figure 1). The blast performance of shell versus matrix configurations was previously studied for aluminized explosives in a chamber [3]. For metal particles in the shell configuration, the tap density was used to determine a metal volume fraction of 55.7% with the voids filled with air.

Figure 3 illustrates the wave diagram for the 2.5 kg spherical matrix and shell configurations. At early times in the near field, the particles overtake the shock front for the interval $0.3 < r < 1.0$ m. The time at which the particles cross the shock occurs later for the shell configuration than for the matrix, and the crossing distance is greater for increasing particle size.

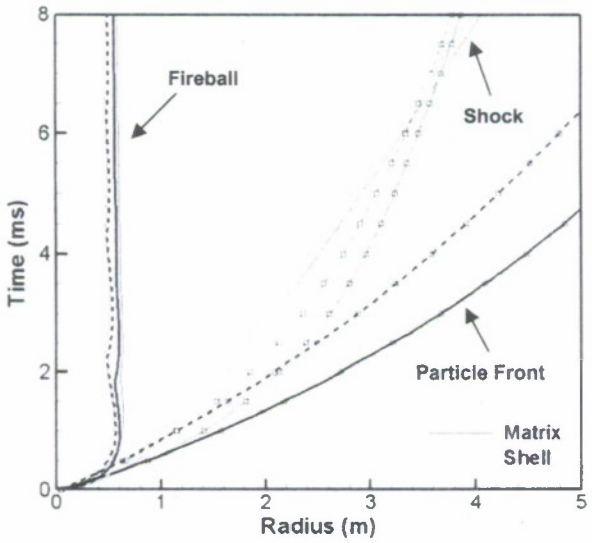

Figure 3: Wave diagram for 2.5 kg spherical tungsten matrix and shell configuration charges. Thick lines, 120 μm; thin lines, 27 μm; solid lines, matrix; dashed lines, shell; black lines, fireball; light blue lines, shock; and, black lines with symbols, particle front.

For the matrix configuration relative to the shell configuration, the shock is slightly farther ahead and the fireball is larger. This is due to the detonation transitioning to an air blast immediately at the end of the charge, without the confinement effect of a dense particle bed. The shell configuration provided more confinement and the fireball recompression is more pronounced and occurs later as indicated in Figure 3. Consequently, the particles in the shell shocked by the detonation are 800 K hotter initially and the dispersed particles in the shell are up to 450 K hotter.

For both particle sizes in general, the far-field dispersed particle front from the matrix configuration is ahead of that for the shell configuration. One exception is the 20 kg charge with small particles, where the dispersed particles from the shell are ahead of the matrix for $r > 3.25$ m. Otherwise, the results obtained for the 20 kg charge exhibit similar behaviour to that of the smaller charge.

3.2 CYLINDRICAL PARTICLE DISPERSAL

Two-dimensional calculations were performed to calculate the dispersal of particles from centrally-initiated cylindrical charges. The blast flow field was expected to feature high directional dependence, particularly in the near-field. Results along a radial slice from the charge centre are compared with spherical dispersal results to study the effect of charge geometry on the blast (Figure 4). This comparison is not simply a change in the degree of blast expansion modelled in one dimension, but rather the full charge shape and expansion is resolved. Only a single cylindrical charge aspect ratio was simulated; results are expected to vary for other charge geometries.

The cylindrical charge has a faster particle front and shock velocity than the spherical result, despite having a smaller initial diameter. In both the spherical and cylindrical charges, the shock and particle fronts are faster for the matrix charges as compared with the shell configuration, although at later times the shock and particle fronts for the shell case eventually pass the equivalent matrix positions.

The cylindrical charge also shows a greater influence of particle distribution (shell versus matrix) on fireball size. The maximum fireball extent for the cylindrical matrix charge is approximately 1.2 m, the fireball extends only 0.6 m in the radial direction for the shell configuration. Reverberations in the fireball evident in the shell configuration are not as distinct in the matrix charge results due to a more diffusive multiphase flow field.

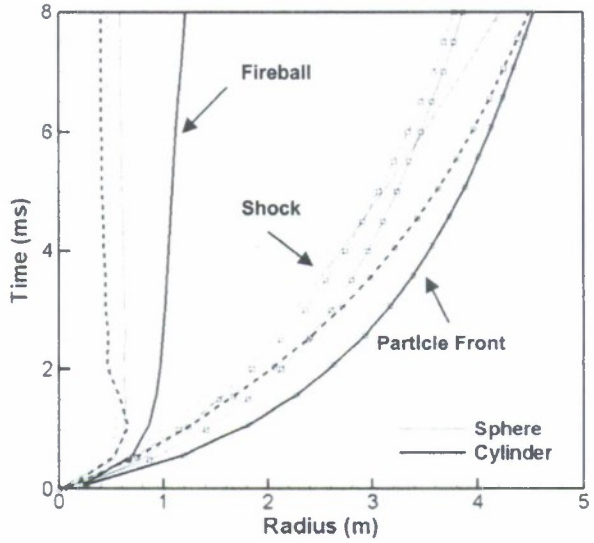

Figure 4: Wave diagram for cylindrical dispersal of 2.5 kg tungsten charges (27 μm diameter). Thick lines, cylindrical charge; thin lines, spherical charge; solid lines, matrix; dashed lines, shell; black lines (no symbols), fireball; light blue lines, shock; and, black lines with symbols, particle front.

Figure 5 shows the strong directional dependence of the cylindrical blast. In particular, the shell case has jetting of detonation products and merging of end shocks with that propagated through the shell. The dense slug of particles originating in the shell travels in a coherent chevron shape which has a confinement effect on the detonation products and the blast. This results in a slower shock speed and more limited radial fireball expansion when compared with the matrix results. In the case of the matrix configuration, the particle front is more dispersed through the domain, although the peak particle concentration is lower. As illustrated in Figure 5, regions of the particle front cross the shock front in the very near field, and result in a slight change in the fluid density ahead of the primary shock. The products jetting from the ends of the charge evident in the shell configuration is not present in the matrix configuration, where the resulting fireball has a shape consistent with a standard cylindrical high explosive charge. The shell versus matrix cylindrical results are also consistent with a previous investigation [3].

Figure 6 illustrates the particle concentration profile along a radial slice from the centre of both spherical and cylindrical charges, while Figure 7 illustrates the particle velocity results along the same lines. Both concentration and velocity are key parameters relevant to PIV (Particle Image Velocimetry) measurement. As also shown in Figure 5, particles originating from a shell are concentrated in a dense slug, whereas the matrix particles are spread over three times the distance. The particle front speed for cylindrical charges is faster than for the spherical charges. While the particle front speed is initially greater for the matrix configuration, the particles configured in a shell eventually overtake the equivalent matrix position. This transition point occurs earlier for the cylindrical charges than for the spherical charges.

Figure 7 illustrates that the particle velocity decreases very quickly with radial distance, from approximately 800 m/s at r = 1-1.5 m to 175 m/s at r = 4 m, while the peak particle concentration decreases roughly 1-1.5 orders of magnitude over the same distance. Changing the particle diameter or material density has the most significant influence on the early-time particle velocity. At 8 ms, the particle velocity is the same for both particle sizes. From the matrix charge, particle velocities in the near-field are faster (50 m/s for 27 μm and 300 m/s for 120 μm), but are similar to the shell at later times.

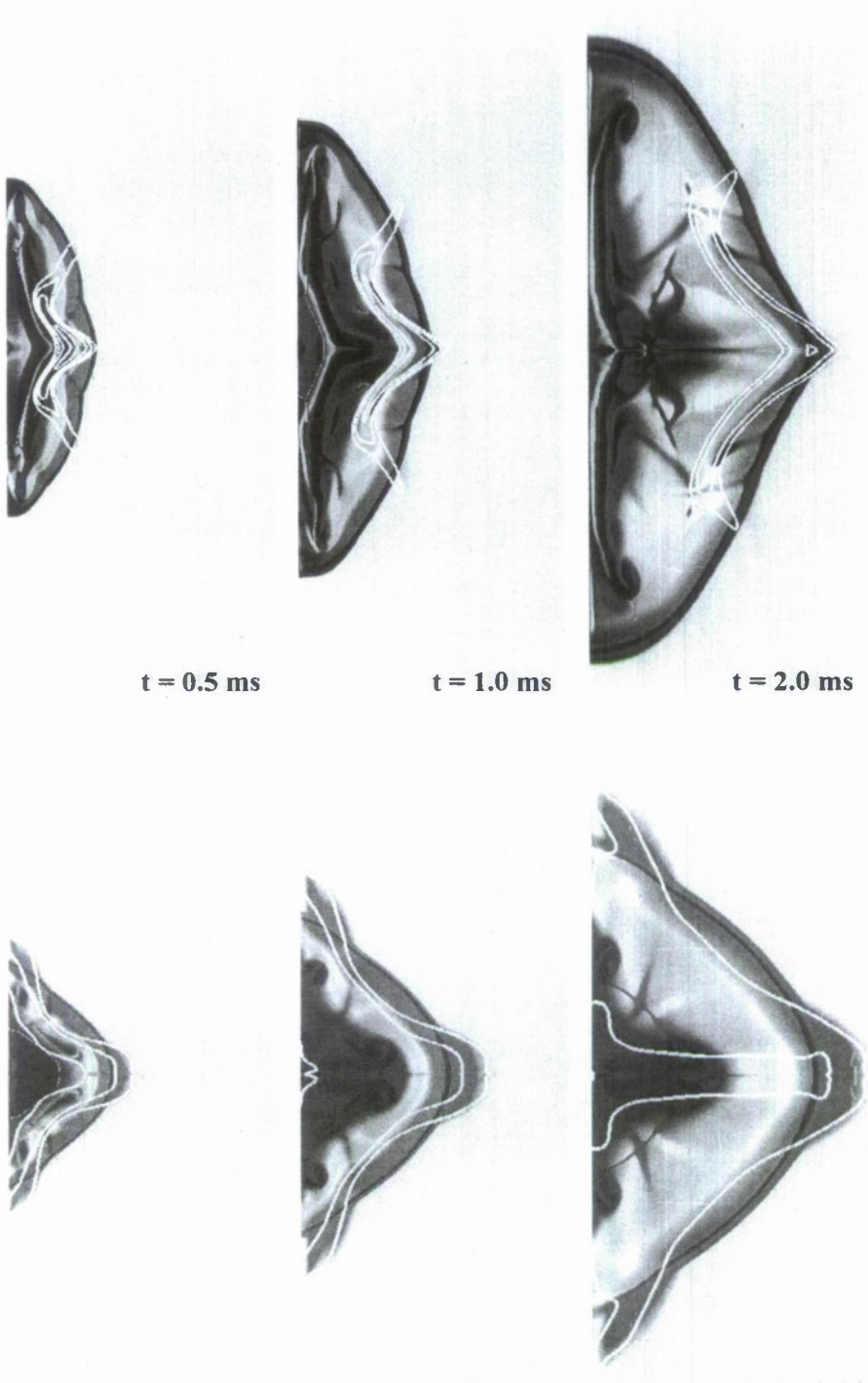

Figure 5: Fluid density (colour) and particle concentration (lines – log) for 27 μm tungsten particles in 2.5 kg (top) shell and (bottom) matrix configurations. Shading indicates strength of density gradient.

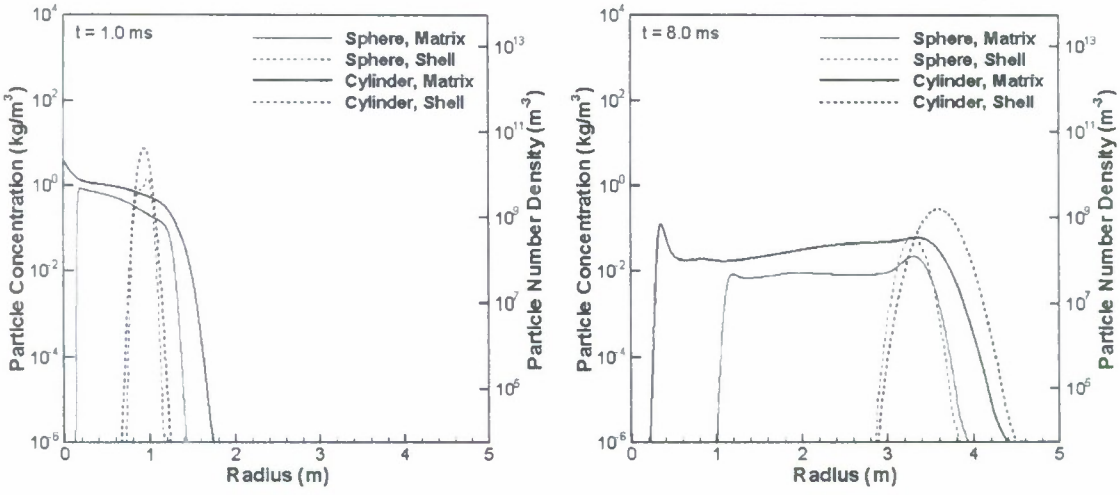

Figure 6: Concentration of dispersed 27 μm tungsten particles in 2.5 kg matrix and shell configurations at (left) t = 1.0 ms and (right) t = 8.0 ms.

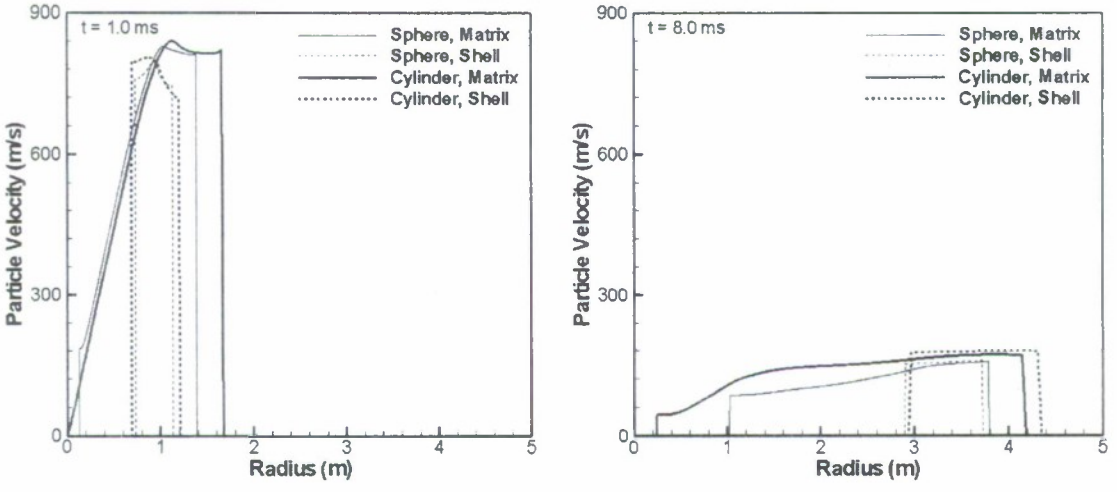

Figure 7: Radial velocity distribution of 27 μm tungsten particles in 2.5 kg matrix and shell configurations at (left) t = 1.0 ms and (right) t = 8.0 ms.

4.0 PRELIMINARY LABORATORY-SCALE INVESTIGATIONS

A series of simulations were performed using the proposed configuration for the experimental trials to be performed at the High Explosives R&D facility at Eglin AFB. Only cylindrical A5 charges surrounded by an annular shell of metal particles were considered. Both tungsten and inert aluminum particles were simulated to investigate the effect of particle size and material density on the dispersal. Figure 8 illustrates the charges used in the experiments with nominal 200 g mass.

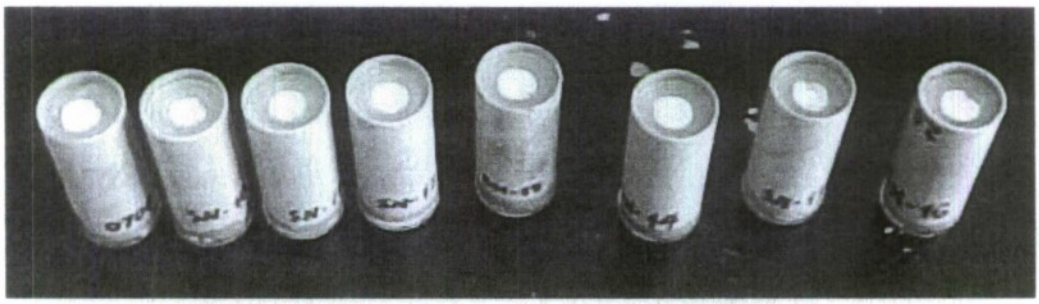

Figure 8: Prepared experimental charges.

4.1 EXPLOSIVE DETAILS

A schematic of the charge is given in Figure 9, with component mass fraction details of the three charges investigated listed in Table 2. All charges involve an A5 explosive core surrounded by a shell of monodisperse particles, with inter-particle voids filled with air. The explosive detonation is initiated by a small region of hot products on the centre axis at one end of the charge.

The volume fraction of air and metal in the shell is relatively constant throughout all charges (approximately 44% air and 56% metal), as is the explosive mass (10.5 g). The densities of A5, tungsten, and aluminum are assumed to be 1650 kg/m^3, 19250 kg/m^3, and 2700 kg/m^3, respectively.

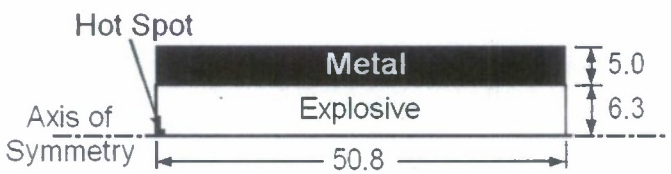

Figure 9: Charge dimensions in millimetres.

Table 2: Charge details

Charge Parameters		Charge Identification Label		
		A5/W-27	A5/W-120	A5/Al-31
Particle Diameter (μm)		27.0	120.0	31.0
Shell Composition (% vol)	Air	44.16	44.16	44.76
	Metal	55.84	55.84	55.24
Total Mass (g)	Explosive	10.5	10.5	10.5
	Metal	151.0	151.0	20.9

4.2 A5/W-27 RESULTS

Select results for the A5/W-27 charge are illustrated in Figures 10-14. The early-time (1-10 ns) detonics phenomena are shown in Figure 10. This image illustrates the explosive detonation, normal and oblique shock transmission into the particle layer, and initial particle layer dispersal pattern. The form of the dispersed particle cloud is affected by both the asymmetric end initiation location, and the open ends of the charge. The spatial particle speed profile is given in Figure 11, and shows that maximum particle speeds of approximately 1500 m/s are located at the ends of the shell, while particle velocities are relatively constant along the outer length of the shell. There is a considerable velocity gradient present through the thickness of the particle cloud, as the particles on the outer edges of the shell are less confined and are thus accelerated more quickly by the shock.

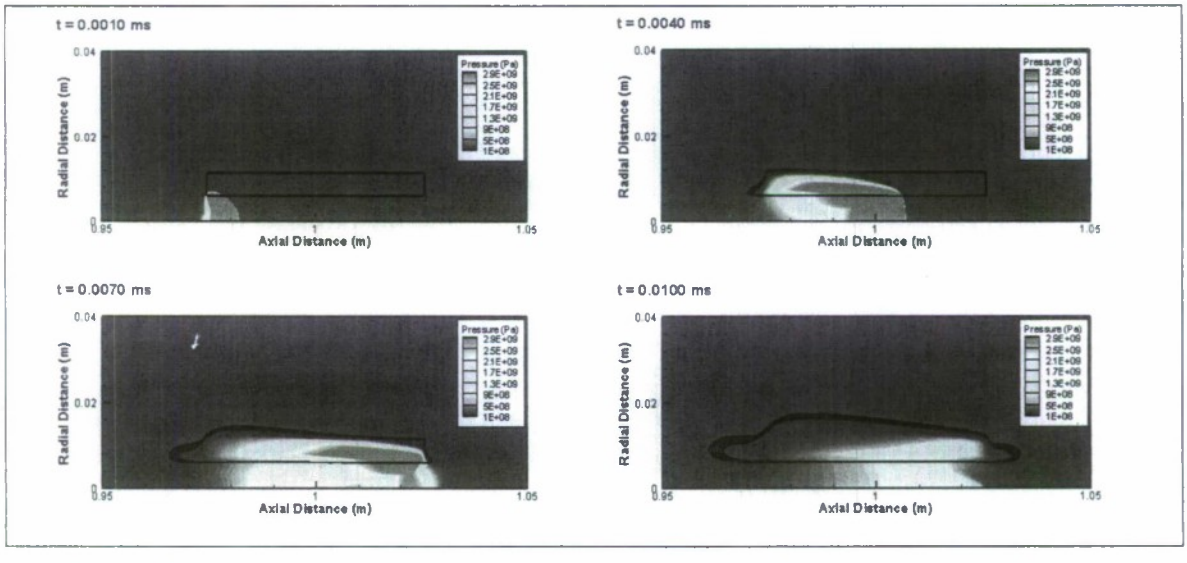

Figure 10: Early-time explosive detonation and particle dispersal of A5/W-27. Flood indicates pressure level; solid lines denote particle concentration of 10 mg/m^3 to 0.1 kg/m^3 (log scale).

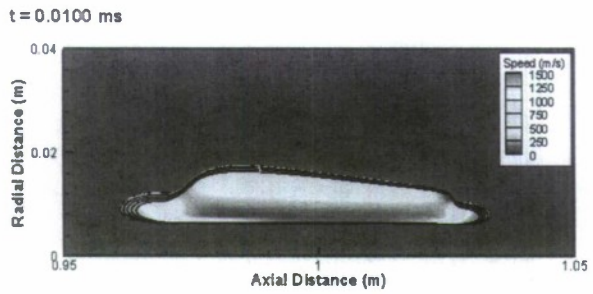

Figure 11: Early-time particle speed profile for A5/W-27. Flood indicates particle speed level; solid lines denote particle concentration of 10 mg/m^3 to 0.1 kg/m^3 (log scale).

Figure 12 illustrates the later-time (first millisecond) particle dispersal and shock pressures. The form of the dispersed particle cloud is quite different than the early-time form shown in Figure 10, with the maximum particle displacements occurring mid-length along the charge. This appears to be due to colliding waves along the charge center, and may be dependent on the charge aspect ratio.

Three coalescing shocks are evident in Figure 12, especially at the later times. These shocks originate from the initial expansion at the initiation end, the shock transmitted through the particle bed, and the transmitted shock out the far end of the tube. Differences in the speeds of these shocks due to changes in the particle bed condition (confinement) are examined in subsequent sections. The results indicate that the incident shock is followed by a second high pressure region at the leading edge of the particle slug, seen most prominently in Figure 12 at t = 1.0610 ms. This may be a ballistic effect, as the high-drag dense particle slug compresses the air ahead of it.

As shown in Figure 13, the peak particle speeds in the bulk of the slug have decayed to approximately half of the earlier-time speeds shown in Figure 11.

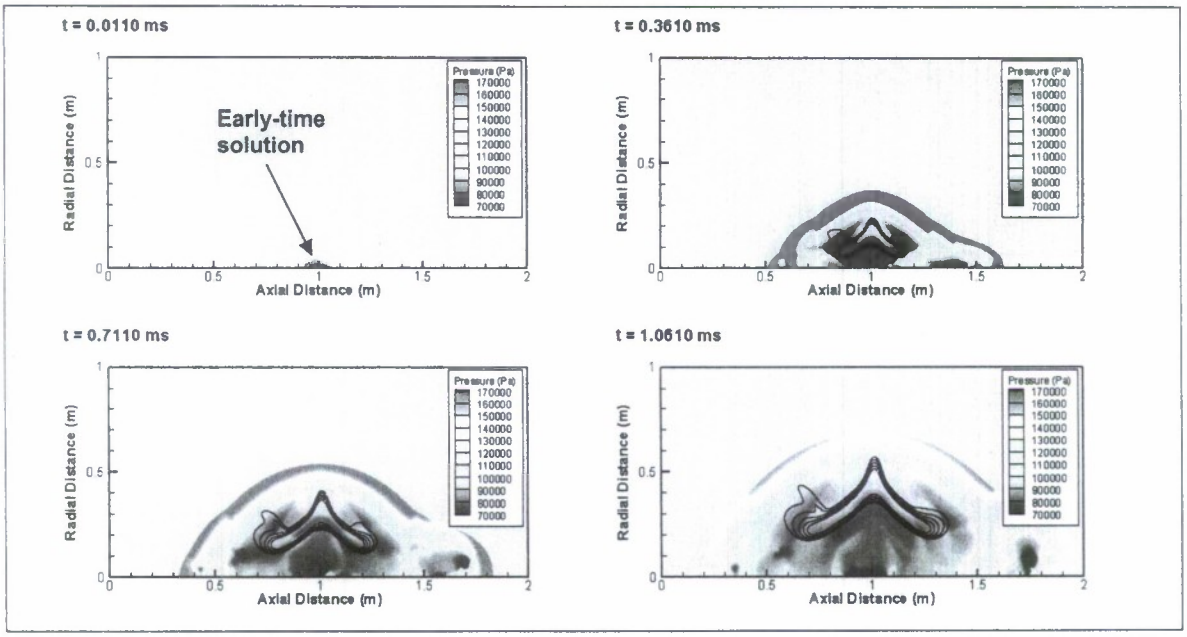

Figure 12: Late-time particle dispersal and shock propagation of A5/W-27. Flood indicates fluid pressure level; solid lines denote particle concentration of 10 mg/m^3 to 0.1 kg/m^3 (log scale).

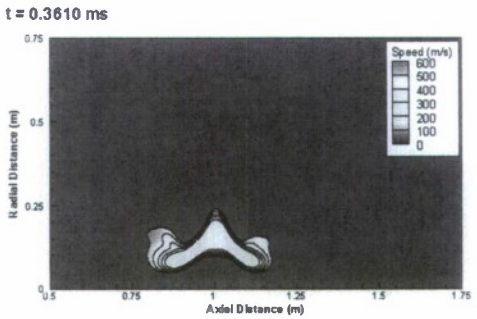

Figure 13: Late-time A5/W-27 particle speed. Solid lines denote particle concentration of 10 mg/m^3 to 0.1 kg/m^3 (log scale).

Numerical gauges were placed at 5 radial distances from the mid-length of the explosive cylinder (r = 0.2, 0.3, 0.4, 0.5 and 0.75 m). Figure 14 plots the pressure and particle number density (number of particles per cubic metre) histories at these locations. The pressure results show a fairly significant second peak, especially at the 0.4 to 0.75 m gauge locations. This second peak is the result of the ballistic shock discussed earlier.

With the definition of a "particle window", number density information can be converted to determine the time-dependent number of particles passing through a volume for later comparison to experimental PIV data.

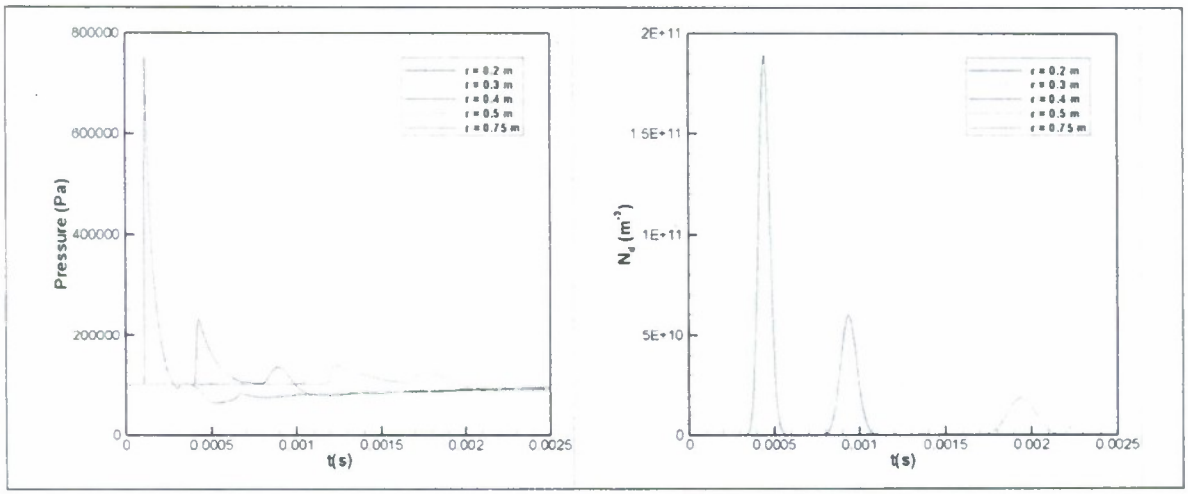

Figure 14: Gauge histories for A5/W-27 (left) Pressure and (right) Particle number density

4.3 A5/W-120 RESULTS

In order to study the effect of particle diameter on the particle dispersal characteristics, simulations were performed with 120 μm tungsten particles while maintaining the same explosive and metal mass fractions. The explosive detonation and early-time dispersal pattern are illustrated in Figure 15. The larger particles require additional time to accelerate as compared to the smaller particles due to the greater inertia.

The resulting lower particle speeds are also very evident with a comparison of Figure 11 and Figure 16, which shows a drop in particle speed as compared with the smaller particles. The velocities in the centre of the slug range from approximately 200-300 m/s in the case of the 120 μm particles, compared with peak particle velocities of approximately 800 m/s at the same location in the 27 μm particle slug. The particle velocities through the thickness are also far more uniform than observed for the small diameter particles.

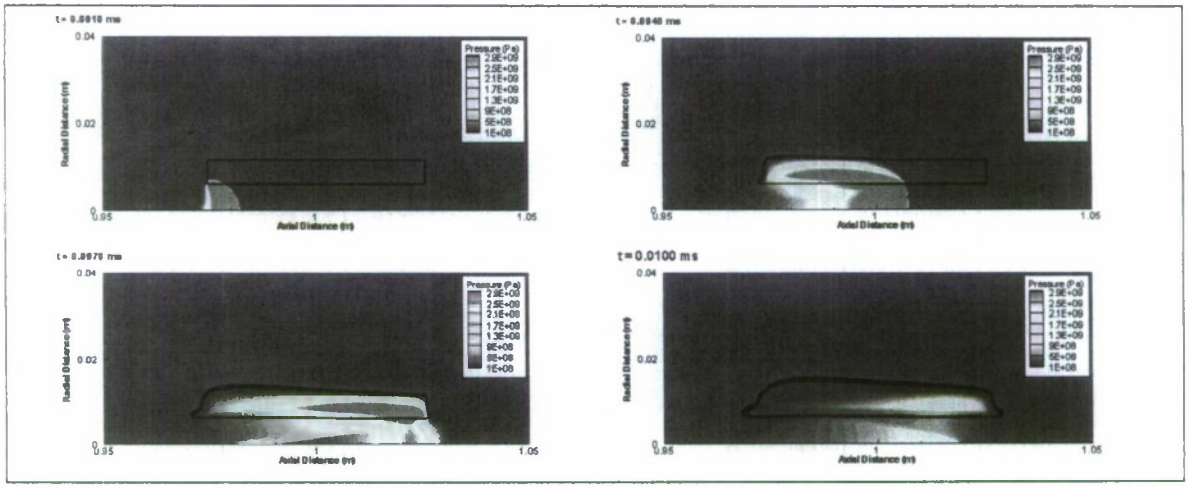

Figure 15: Early-time explosive detonation and particle dispersal of A5/W-120. Flood indicates fluid pressure level; solid lines denote particle concentration of 10 mg/m^3 to 0.1 kg/m^3 (log).

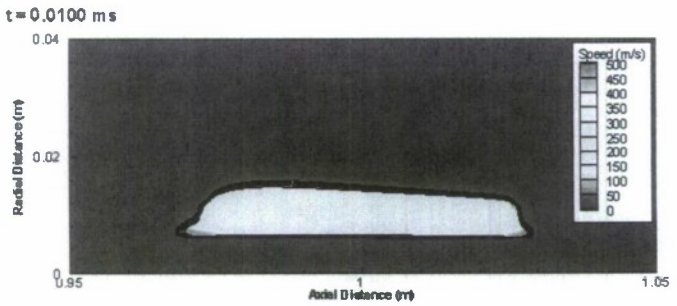

Figure 16: Early-time particle speed profile for A5/W-120. Flood indicates particle speed level; solid lines denote particle concentration of 10 mg/m^3 to 0.1 kg/m^3 (log).

The later-time pressure and particle concentration profiles for the A5/W-120 charge are illustrated in Figure 17. The radial shock speed is greater for the larger particle size due to lower overall drag forces compared to the smaller particles. Although the drag of an individual large particle is greater than the drag of a smaller particle, the total drag on a cloud of large diameter particles is lower than for an equal volume fraction of small particles, therefore influencing the strength of the shock transmitted through the particle layer.

While the radial shock strength is increased for the larger particles, the end shock speeds are reduced. It is hypothesized that this is due to the increased confinement effect of the small particles. Drag forces are greater for the shell of smaller particles, also resulting in a greater confining force. As a consequence of the greater confinement, higher strength and faster shocks expand from the ends of the charge in the case of the smaller diameter particles. This theory also explains the absence of the ballistic shock present in the small diameter results. Because of the lower particle cloud drag forces, the strength of the compression wave ahead of the particle cloud is also reduced.

Figure 17 also illustrates the reduced displacement of the large diameter particle cloud as compared with the cloud of small particles (Figure 12). The slug of small particles has high total drag forces and low inertia, and therefore the small particles are accelerated more quickly. These timeframes occur relatively early in the overall expansion, and it is anticipated that after sufficient time, the large diameter particles will overtake the small particle position, as shown fundamentally in Figure 1 ($r < 1$ m). As shown in Figure 18, the average particle speeds for the large diameter particles is still lower than the small particle speeds.

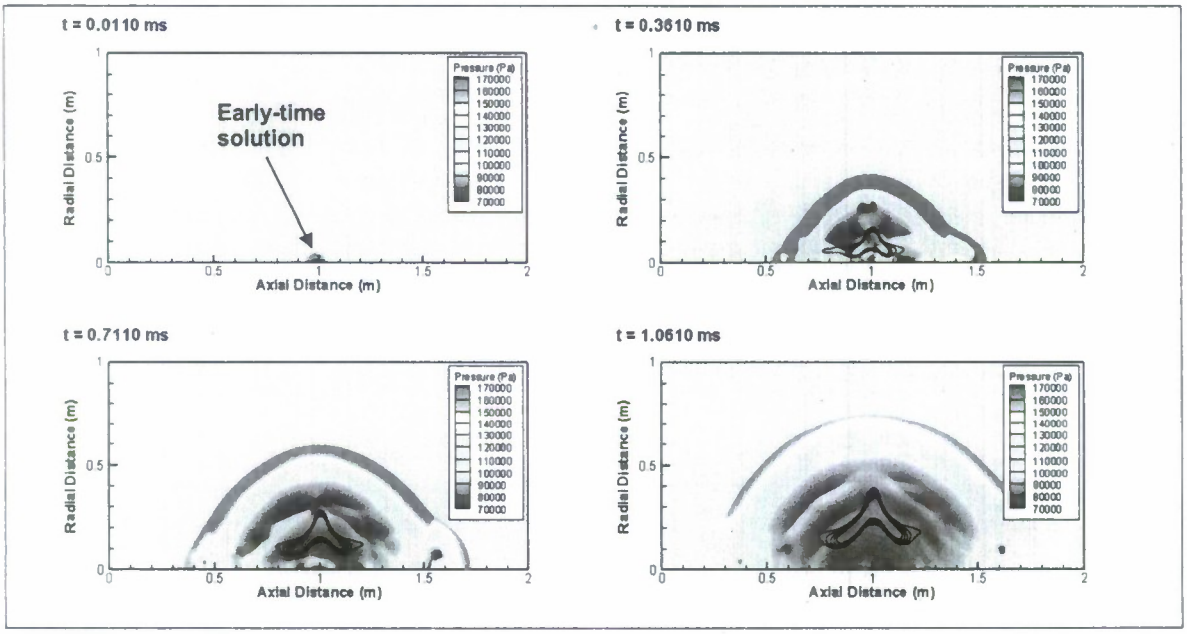

Figure 17: Late-time particle dispersal and shock propagation of A5/W-120. Flood colour indicates fluid pressure level; solid lines denote particle concentration of 10 mg/m^3 to 0.1 kg/m^3 (log scale).

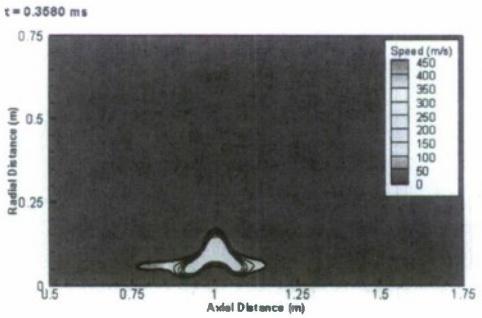

Figure 18: Late-time A5/W-120 particle speed. Solid lines denote particle concentration of 10 mg/m^3 to 0.1 kg/m^3 (log scale).

Figure 19 gives the numerical gauge results for five measurement locations in the radial direction. The faster radial shock speed is evident when comparing to Figure 14, and the

second pressure peak due to the ballistic shock does not occur with the larger particles. The relative particle number density trends are very similar to the small particle results, however the number densities are several orders of magnitude lower due to the reduced number of particles in the shell. Specifically, there should be 90 times the number of smaller particles per unit volume as larger particles.

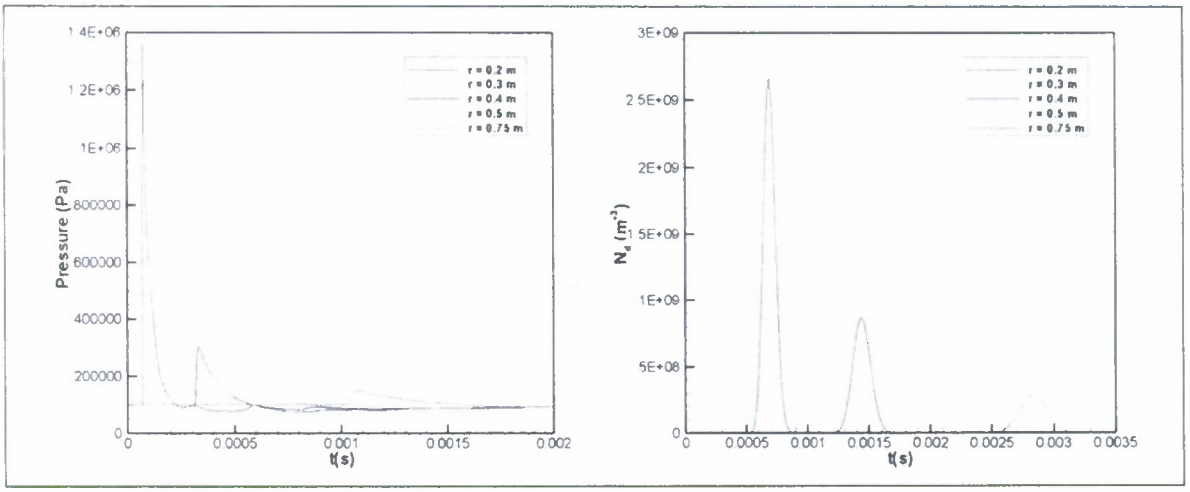

Figure 19: Gauge histories for A5/W-120 (left) Pressure and (right) Particle number density

4.4 A5/AL-31 RESULTS

The effect of particle material density was investigated through simulations involving inert aluminum particles. The aluminum particles were modelled as inert to remove potential reactivity effects from the analysis and focus on particle material effects only. The 31 μm aluminum particles were of comparable size to the 27 μm tungsten particles, however represented only approximately 14% of the tungsten particle mass. Figure 20 illustrates the detonation propagation, oblique shock formation, and particle dispersal for the first 0.01 ms. The particle layer disperses much more quickly than in either of the tungsten cases, due to the reduced particle inertia. The particles have been dispersed to approximately twice their original radius before the detonation reaches the end of the charge. The particle speeds are approximately double those observed for the small tungsten particles, as shown in Figure 21.

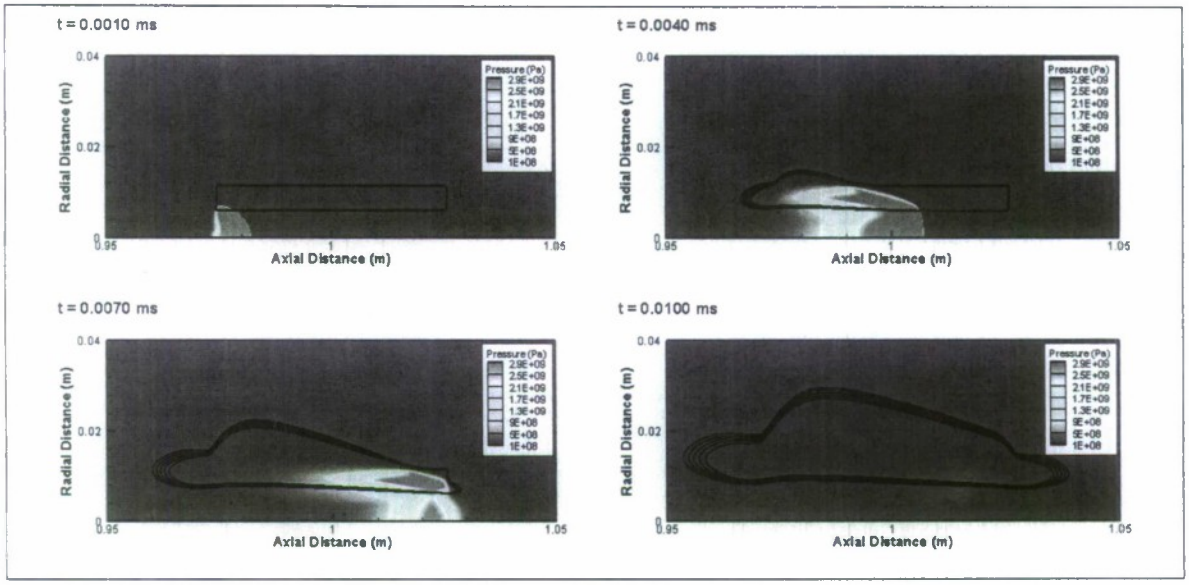

Figure 20: Early-time explosive detonation and particle dispersal of A5/Al-31. Flood indicates fluid pressure level; solid lines denote particle concentration of 10 mg/m^3 to 0.1 kg/m^3 (log scale).

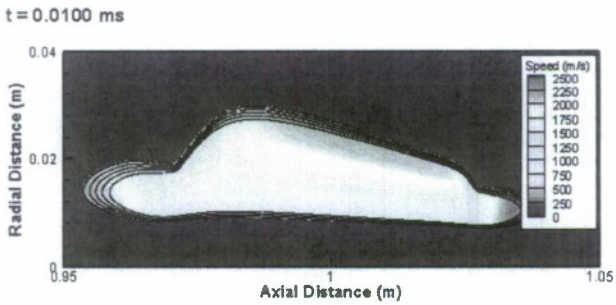

Figure 21: Early-time particle speed profile for A5/Al-31. Flood indicates particle speed level; solid lines denote particle concentration of 10 mg/m^3 to 0.1 kg/m^3 (log scale).

Figure 22 illustrates the pressure and particle concentration contours for times between 0.01 and 1.0 ms. In contrast to the tungsten particle results, the aluminum particle cloud travels with the leading shock, with some particles travelling ahead of the shock. The results show leading trails of low concentration particles that begin at early time due to detonation pressures and dense drag forces at the corners of the shell. These may be numerical artifacts and should be investigated further. The radial shock speed is greater than for the 27 μm tungsten particles, and there appears to be lower confinement given the relative shock strengths along the axis of symmetry. This seems to indicate that the lower mass and lower inertia particle shell results in greater acceleration and a net decrease in the drag force.

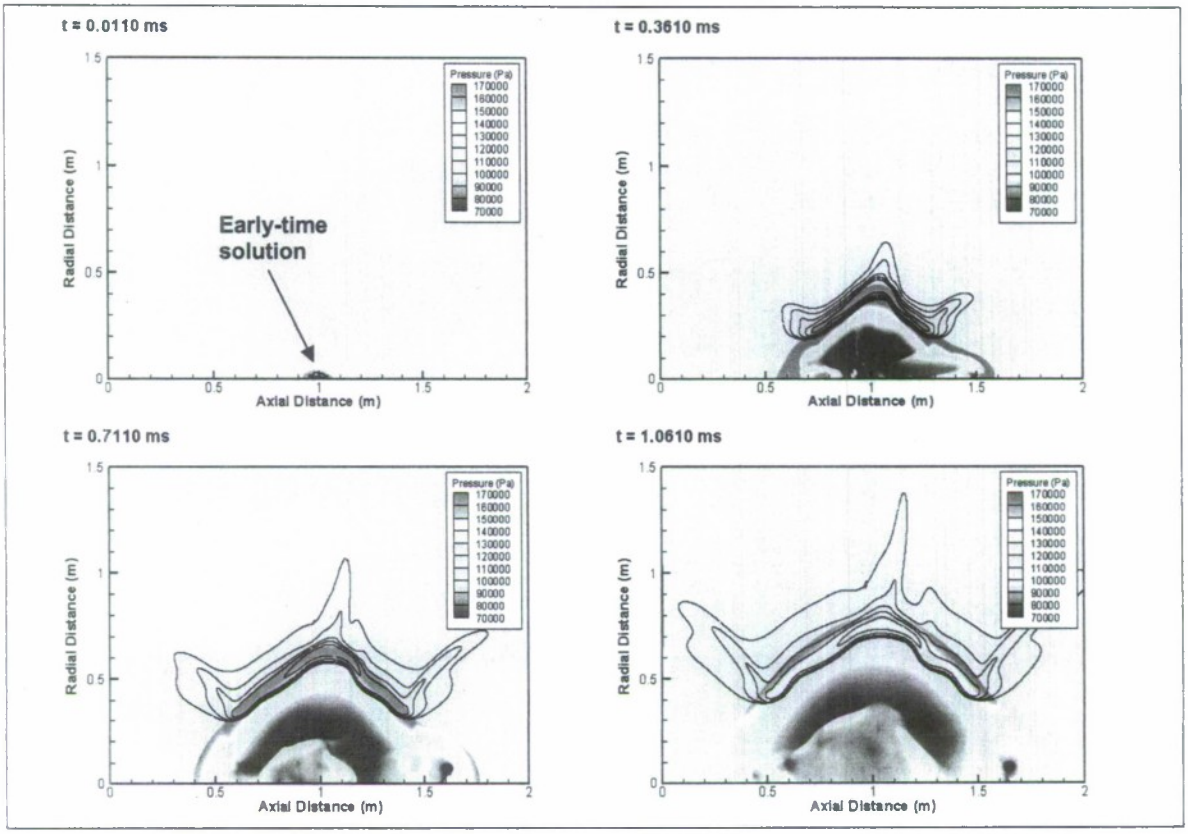

Figure 22: Late-time particle dispersal and shock propagation of A5/Al-31. Flood indicates fluid pressure level; solid lines denote particle concentration of 10 mg/m^3 to 0.1 kg/m^3 (log scale).

Figure 23 illustrates the particle speeds at 0.36 ms. The aluminum results appear to show a large difference in velocity at the centre of the particle cloud between the inner and outer surfaces, however the area with large speed (approximately 1500 m/s) occurs in a region with a relatively low particle concentration.

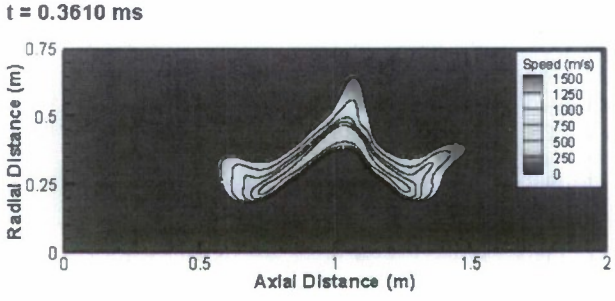

Figure 23: Late-time A5/Al-31 particle speed. Solid lines denote particle concentration of 10 mg/m^3 to 0.1 kg/m^3 (log scale).

The pressure and particle number density histories at five numerical gauge locations are plotted in Figure 24. The secondary shock which is most pronounced at 0.2 m appears to not be due to a ballistic-type shock as observed in the 27 μm tungsten case, but is due rather to a secondary recompression fluid shock (as seen in Figure 22). This wave may be stronger than in either of the tungsten cases as the particle cloud travels with the incident shock, and the second wave is not impeded by a lagging particle cloud.

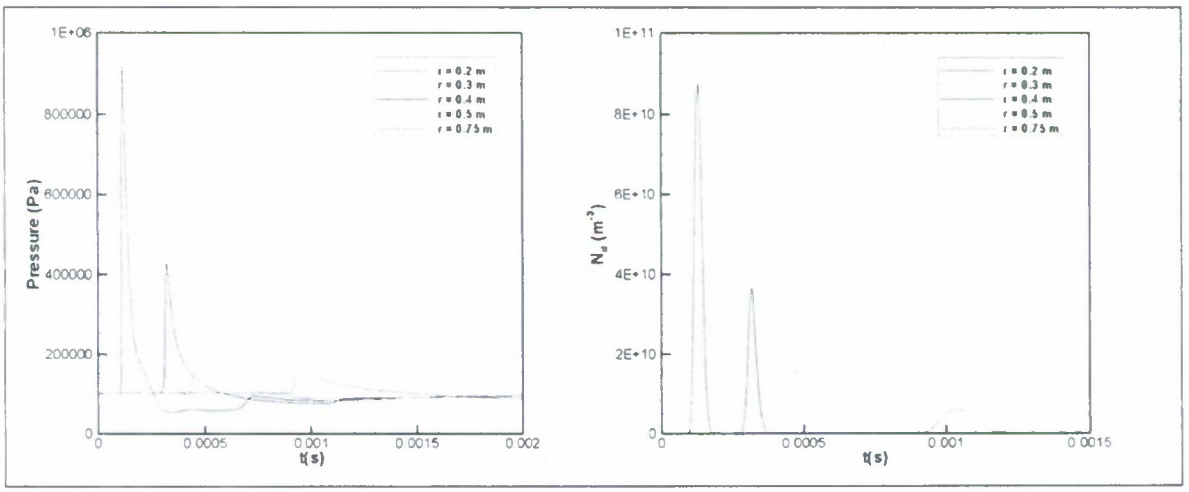

Figure 24: Gauge histories for A5/Al-31 (left) Pressure and (right) Particle number density

5.0 DISCUSSION/CONCLUSIONS

In the current study, the explosive dispersal of densely-packed metal particles in cylindrical RDX-based charges was studied numerically in support of experimental trials. Simulations were conducted using *Chinook*, a reactive multiphase CFD code.

Fundamental studies involving large-scale explosives were performed to show scaling phenomena while avoiding potential initiation and critical diameter effects. Spherical tungsten particles were applied in high metal mass fraction cylindrical and spherical charges in two fundamental configurations: a particle matrix uniformly embedded in a solid explosive versus an annular shell of particles surrounding a high-explosive core. The effect of particle number density was investigated by varying the nominal particle diameter from 27 to 120 μm while maintaining a constant metal mass fraction. Results were compared with steel particles to evaluate the influence of material density on dispersal. The dispersal dynamics are recorded on wave diagrams and are observed at radial locations in terms of arrival time, velocity and particle concentration.

Preliminary laboratory-scale simulations were performed using the anticipated experimental configuration for the High Explosives R&D facility at Eglin AFB trials. The effect of particle size and density were investigated, and information to assist in the experiments was obtained. Results were consistent with the fundamental study involving the large-scale explosives, particularly the shape of the cylindrical dispersed dense particle slug, and the relative performance of the large and small particles.

Particle temperature information is available to estimate aluminum reactivity in blast flows. The influence of other factors such as particle shape, size distribution and initiation location may be investigated in the future. The initial momentum transfer is accounted for in the current simulations by applying a momentum acceleration factor to the particle drag force for a short duration during the detonics and near field phases. To improve the predictability of early time particle loading, the momentum acceleration factor developed for shock and detonation interaction with packed metal particles will be employed in the future.

6.0 REFERENCES

[1] Zhang, F., Frost, D.L., Thibault, P.A., and Murray, S.B., Explosive Dispersal of Solid Particles, *Shock Waves*, **10**: 431-443 (2001).

[2] Frost, D. L., Goroshin, S., Levine, J., Ripley, R. C., and Zhang F., Critical Conditions for Ignition of Aluminum Particles in Cylindrical Explosive Charges, *Shock Compression of Condensed Matter – 2005*, pp. 972-975 (2006).

[3] Ripley, R.C., Donahue, L., Dunbar, T.E., and Zhang, F., Explosion performance of aluminized TNT in a chamber, *Proc. 19th Military Aspects of Blast and Shock*, Calgary, Canada (2006).

[4] Toro, E.F. (1997) Riemann Solvers and Numerical Methods for Fluid Dynamics, Springer-Verlag.

[5] Batten, P., Clark, N., Lambert, C. and Causon, D. M.., On the choice of wavespeeds for the HLLC Riemann solver, SIAM J. Sci. Comput., **18**(6), pp. 1553-1570, Nov 1997.

[6] Zhang, F., Tran, D. and Thibault, P. A., Multiphase models for detonation propagation in a dusty or porus medium, Combustion Canada '96, Ottawa, Ontario, June 1996.

[7] Baer, M. R. and Nunziato, J. W., A two-phase mixture theory for the deflagration-to-detonation transition (DDT) in reactive granular materials, *Int. J. Multiphase Flow*, **12**, pp. 861-889, 1986.

[8] Mader, C. L., *Numerical Modeling of Explosives and Propellants*, 2nd Ed., CRC Press, Boca Raton, Florida, 1998.

[9] Walsh, J. M. and Christian, R. H. Equation of state of metals from shock wave measurements, *Physical Review*, **97**(6), pp. 1544-1556, 1955.

[10] Lee, E. L., Hornig, H. C. and Kury, J. W., Adiabatic expansion of high explosive detonation products, *UCRL-50422*, Lawrence Livermore Laboratory, University of California, 1968.

[11] Fried, L. E., Howard, W. M., and Souers, P.C., "Cheetah 2.0 User's Manual," *UCRL-MA-117541* (Revision 5), Lawrence Livermore National Laboratory, 1998.

[12] Ripley, R.C., Zhang, F., and Lien, F.-S., "Detonation Interaction with Metal Particles in Explosives," *Proc. 13th International Detonation Symposium*, Norfolk, VA (2006).

[13] Richards, D.W., De Angelis, R.J., Kramer, M.P., House, J.W., Cunard, D.A., and Shea, D.P., "Shock-Induced Deformation of Tungsten Powder", *Adv. X-ray Analysis*, **47**, 351-356 (2004).